Spiral vortices traveling between two rotating defects in the Taylor-Couette system

Ch. Hoffmann, M. Lücke, and A. Pinter
Institut für Theoretische Physik, Universität des Saarlandes, D-66041 Saarbrücken, Germany
(Received 16 May 2005; revised manuscript received 16 August 2005; published 8 November 2005)

Numerical calculations of vortex flows in Taylor-Couette systems with counter rotating cylinders are presented. The full, time-dependent Navier-Stokes equations are solved with a combination of a finite difference and a Galerkin method. Annular gaps of radius ratio $\eta=0.5$ and of several heights are simulated. They are closed by nonrotating lids that produce localized Ekman vortices in their vicinity and that prevent axial phase propagation of spiral vortices. The existence and spatiotemporal properties of rotating defects, modulated Ekman vortices, and the spiral vortex structures in the bulk are elucidated in quantitative detail.

DOI: 10.1103/PhysRevE.72.056311 PACS number(s): 47.20.−k, 47.32.−y, 47.54.+r, 47.10.+g

I. INTRODUCTION

The spontaneous appearance of spiral vortices in the annular gap between the concentric rotating cylinders of the Taylor-Couette system [1–4] has stimulated research activities [5–24] ever since their prediction [25] and their first observation [26]. Spiral vortex structures bifurcate, like the competing toroidally closed Taylor vortices out of the rotationally symmetric and axially homogeneous basic state of circular Couette flow (CCF), albeit at different bifurcation thresholds [12,24]. The Taylor vortex flow (TVF) is rotationally symmetric and stationary while the spiral vortex flow (SPI) breaks the rotational symmetry of the annular gap. It oscillates globally in time by rotating azimuthally as a whole, thereby propagating axially.

The spiral pattern is effectively one dimensional, like TVF. It is also stationary when seen from a co-moving frame [6]: The spiral fields do not depend on time t, axial coordinate z, and azimuthal angle φ separately but only via the combined phase variable $\phi=kz+M\varphi-\omega(k,M)t$. Here k and M are the axial and azimuthal wave numbers, respectively, and ω is the frequency. In the φ-z plane of an "unrolled" cylindrical surface, the lines of constant phase ϕ are straight. An azimuthal wave number $M>0$ implies a left-handed spiral (L-SPI) while $M<0$ refers to right-handed spirals (R-SPI) with our convention of taking k to be positive. L-SPI and R-SPI are mirror images of each other under the operation $z\rightarrow -z$ and are symmetry degenerate flow states. Which of them is realized in a particular experimental or numerical setup depends on initial conditions and parameter history.

With the lines of the constant phase in the φ-z plane being oriented for both spiral types obliquely to the azimuthal "wind" of the basic CCF, both spirals are advectively rotated by the latter like rigid objects. The direction of the common angular velocity $\dot{\varphi}_{SPI}=\omega(k,M)/M$ is the one of the inner cylinder's rotation rate [24], which we take to be positive. Due to the advection enforced rigid-body rotation of the spiral vortices, the phase of a L-SPI ($M>0$) is propagated axially upward and that of a R-SPI ($M<0$) downward. Thus, the oscillatory flow structure of so-called ribbons consisting of an equal amplitude nonlinear combination of L-SPI and R-SPI rotates azimuthally but does not propagate axially [6]. On the other hand, the rotationally symmetric ($M=0$) structure of toroidally closed Taylor vortices is stationary; being parallel to the azimuthal CCF, the latter cannot advect these vortices.

Strictly speaking the axially homogeneous CCF and the TVF and SPI structures exist with axially homogeneous amplitudes only in the theoretical idealizations of axially unbounded or axially periodic systems. Translational symmetry breaking conditions at the top and bottom end of the annulus generate (mostly local) deviations in the basic state flow as well in the above-mentioned vortex structures. For example, the experimentally often used rigid nonrotating lids that close the annular gap enforce for any driving the well-known stationary, rotationally symmetric Ekman vortices close to the lids [23,27–30]. Their spatially varying wave number and amplitude profile distinguishes them from the TVF structure with axially homogeneous profiles.

In a sufficiently long system, the Ekman vortex structures close to the lids smoothly connect and transform to a bulk TVF structure, both patterns being stationary with the common azimuthal wave number $M=0$. So then the question is: How do rotating and axially propagating SPI vortices with $M\neq 0$ arise in the bulk when the nonpropagating Ekman vortex structures being fixed at the lids prevent phase propagation there? This is basically the problem that we elucidate here, using numerical simulations of the full (three-dimensional) 3D Navier-Stokes equations (NSE). Surprisingly, it does not seem to have been addressed in such detail in the literature.

However, the influence of a finite system size on a traveling pattern such as SPI vortex flow has been explored, albeit from a more general point of view [9,15,16,31]. Also, the dramatic effects of nonrotating rigid lids on the flow in rather short Taylor-Couette systems have been investigated in detail for setups where the vortex structures show strong axial variations [21,32].

Our paper is organized as follows: In Sec. II we introduce the notation, the control parameters, the basic equations, and the method used to simulate the Taylor-Couette system. Section III contains our results concerning the transient dynamics of spiral generation, the steady state structure and dynamics, in particular, of the rotating defects, and the stability of SPI flow. The last section contains the conclusion.

II. SYSTEM AND THEORETICAL DESCRIPTION

We present numerical results for the vortex flow in Taylor-Couette systems with counterrotating cylinders. The radius ratio r_1/r_2 of the inner to outer cylinder is $\eta=0.5$. Various aspect ratios $\Gamma=L/d$ of cylinder length L to gapwidth $d=r_2-r_1$ are considered in the range $5\leqslant\Gamma\leqslant 16$. The fluid in the annulus is taken to be isothermal and incompressible with kinematic viscosity ν. To characterize the driving of the system, we use the Reynolds numbers

$$R_1 = r_1\Omega_1 d/\nu, \quad R_2 = r_2\Omega_2 d/\nu. \tag{2.1}$$

They are the reduced azimuthal velocities of the fluid at the inner and outer cylinder, respectively, where Ω_1 and Ω_2 are the respective angular velocities of the cylinders. The inner one is always rotating counterclockwise so that Ω_1 and R_1 are positive.

Throughout this paper we measure lengths in units of the gapwidth d. The momentum diffusion time d^2/ν radially across the gap is taken as the time unit. Thus, velocities are reduced by ν/d. With this scaling, the NSE take the form

$$\partial_t \mathbf{u} = \boldsymbol{\nabla}^2\mathbf{u} - (\mathbf{u}\cdot\boldsymbol{\nabla})\mathbf{u} - \boldsymbol{\nabla}p. \tag{2.2}$$

Here p denotes the pressure reduced by $\rho\nu^2/d^2$ and ρ is the mass density of the fluid. Using cylindrical coordinates, the velocity field

$$\mathbf{u} = u\mathbf{e}_r + v\mathbf{e}_\varphi + w\mathbf{e}_z \tag{2.3}$$

is decomposed into a radial component u, an azimuthal one v, and an axial one w.

The NSE were solved numerically with a finite difference method in the r-z plane combined with a spectral decomposition in φ

$$f(r,\varphi,z,t) = \sum_{m=-m_{max}}^{m_{max}} f_m(r,z,t)e^{im\varphi}. \tag{2.4}$$

Here f denotes one of $\{u,v,w,p\}$ and $m_{\max}=8$ was chosen for an adequate accuracy. To simulate annuli that are bounded by stationary lids at $z=0$ and $z=\Gamma$ we imposed no-slip boundary conditions.

The calculations were done on homogeneous staggered grids with common discretization lengths $\Delta r=\Delta z=0.05$, which have shown to be more accurate than nonhomogeneous grids. Time steps were always well below the von Neumann stability criterion and by more than a factor of 3 below the Courant-Friederichs-Lewy criterion (cf. [24] for details of the numerical calculations). From various control calculations done with different $m_{\max}$ and/or grid spacings, we conservatively conclude that typical SPI frequencies have an error of less than about 0.2% and that typical velocity field amplitudes can be off by about 3–4%. Furthermore, good agreement with experimental spirals was found (cf. Figs. 8 and 9 of [24]).

For diagnostic purposes we also evaluated the complex mode amplitudes $f_{m,n}(r,t)$ obtained from a Fourier decomposition in axial direction

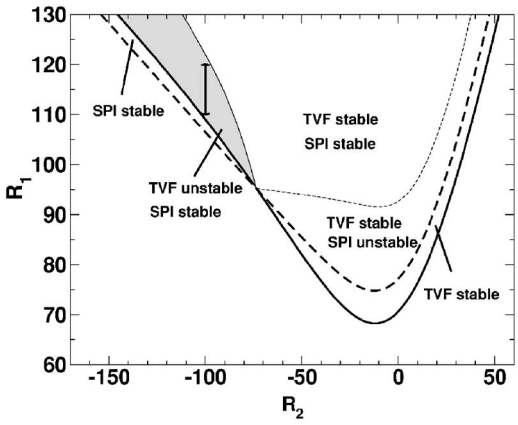

FIG. 1. Phase and stability diagram of TVF ($M=0$) and SPI ($M=\pm 1$) solutions subject to axially periodic boundary conditions imposing the axial wavelength $\lambda=1.6$. Thick full (dashed) line denotes the bifurcation threshold for the TVF (SPI) solution out of CCF. Vertical bar indicates the range of R_1 values for which simulations of finite length systems with rigid stationary lids are presented.

$$f_m(r,z,t) = \sum_n f_{m,n}(r,t)e^{in(2\pi/\Gamma)z}. \tag{2.5}$$

Note that m is the index of a particular azimuthal mode occurring in the representations (2.4) and (2.5), while we use M to identify the azimuthal wave number of a particular solution. So, for example, a $M=-1$ flow state is a R-SPI with an azimuthal wave number $M=-1$ that will contain in general several m modes.

III. RESULTS

For our finite-length annuli with stationary lids at their ends we kept the outer cylinder rotation Reynolds number fixed at $R_2=-100$. Results were obtained for R_1 in the range $110\leqslant R_1\leqslant 120$ that is marked by a vertical bar in Fig. 1.

This figure shows for reference purposes the phase and stability diagram of TVF ($M=0$) and SPI ($M=\pm 1$) solutions subject to axially periodic boundary conditions. The range $110\leqslant R_1\leqslant 120$ to be explored here lies in a control parameter region where both SPI and TVF solutions exist, with the former (latter) being stable (unstable) under periodic boundary conditions. The bifurcation thresholds out of the CCF lie at $R_1=106.5$ for SPI and at $R_1=108.9$ for TVF.

Strictly speaking these axially periodic solutions do not exist in systems of finite axial length that are bounded by rigid lids. Ekman vortices [23,27–30] always appear subcritically near the lids with a spatially varying wave number and amplitude profile that distinguishes them from the homogeneous TVF structure. Also, the SPI flow can be realized with constant amplitude and wave number only in the bulk at a sufficiently large distance from the lids.

A. Transient dynamics of spiral generation in the bulk

Here we show how spirals occur in the bulk of a $\Gamma=12$ system as a representative example of commonly used setups

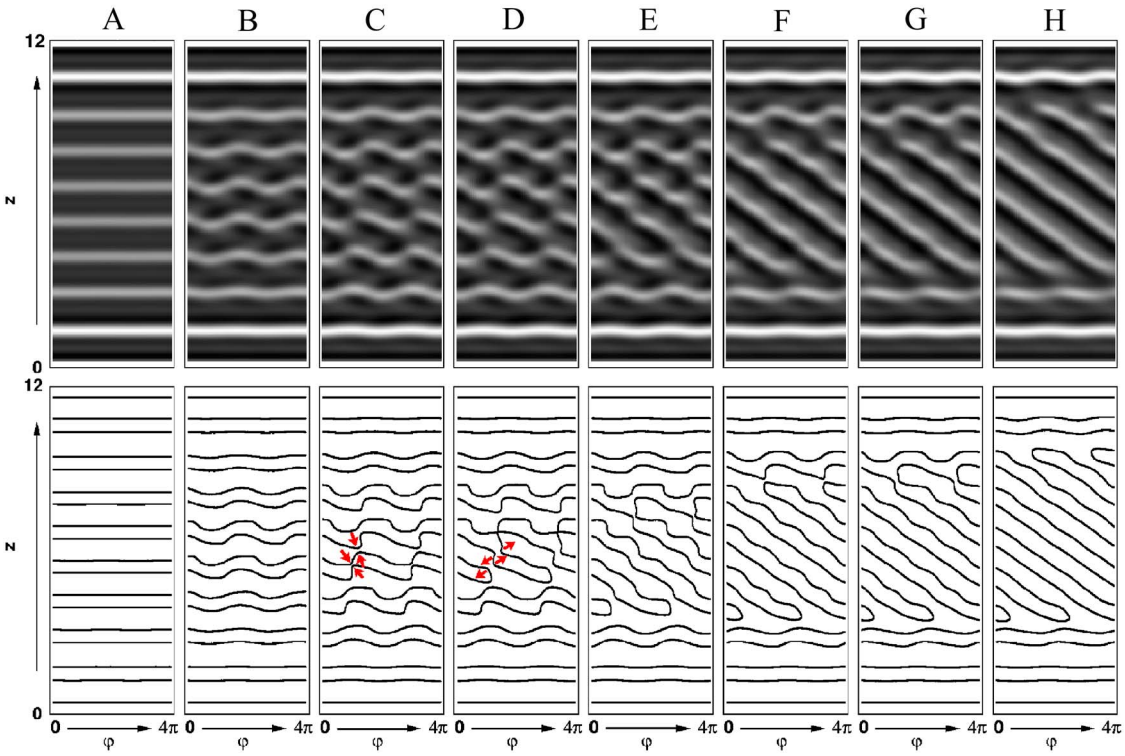

FIG. 2. (Color online) Snapshots of the time evolution toward the L-SPI flow in the bulk. The snapshot times A to H are indicated in Fig. 3. The top row shows the radial velocity field u in an unrolled cylindrical φ-z surface at midgap by gray scale plots with white (black) denoting radial out (in) flow. The bottom row shows the node positions of u. For better visibility the plots are periodically extended to an azimuthal interval of 4π. The initial condition is the fluid at rest plus infinitesimal white noise in all velocity fields. Final Reynolds numbers are $R_1=110$, $R_2=-100$, aspect ratio $\Gamma=12$.

in experiments. We start from the rest state—to be precise—from the quiescent fluid plus infinitesimal white noise in all velocity fields. The rotation rates of the cylinders are then stepped up instantaneously to supercritical final values of R_1 and R_2 for which the SPI flow is stable and TVF is unstable under axially periodic boundary conditions, cf. Fig. 1. Step up from a subcritical driving entails a similar transient.

1. Front propagation of unstable TVF into unstable CCF

Figures 2 and 3 show the long-term evolution of the flow for the case of $R_1=110$ which lies about 1% (2%) above the TVF (SPI) threshold. However, first the unstable CCF flow is growing radially in the bulk and simultaneously, the Ekman vortices are growing near the lids [33]. Both occur on a fast time scale of about one to two radial diffusion times, which are not resolved in Figs. 2 and 3. The TVF fronts are propagating axially into the bulk from the Ekman vortex structures near the lids [33]. Note that $M=0$ TVF can grow at supercritical driving independent of its stability behavior. So here we have a front of an unstable structured state that propagates into an unstable unstructured one. The velocity of the TVF fronts is rather large progressing at least five gapwidths per unit diffusion time. After about five diffusion times, the fully developed unstable TVF is established with homogeneous amplitude and wave number profile in the bulk in equilibrium with the axially varying Ekman vortex structures near the lids, cf. column A of Fig. 2. This TVF growth scenario is dominated by the large deterministic forces that drive the Ekman vortex flow near the lids and thus is largely insensitive to the small initial noise.

2. Transformation of unstable TVF into stable SPI flow

Starting with this TVF configuration, we illustrate in Fig. 2 the further time evolution of the vortex flow. To that end, we show in the top snapshots of the radial velocity field u in

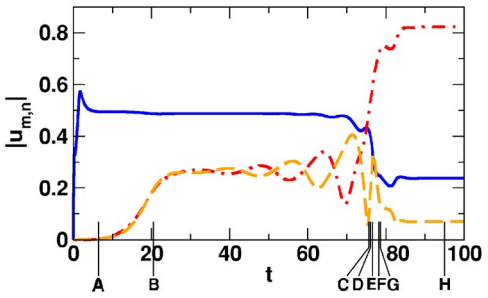

FIG. 3. (Color online) Time evolution of the dominant mode amplitudes $|u_{m,n}|$ (2.5) of the radial velocity field at midgap. Shown is the transient toward the L-SPI flow in the bulk that is documented in Fig. 2 by snapshots. Full line: TVF mode $m=0$, dashed dotted line: L-SPI mode $m=1$, and dashed line: R-SPI mode $m=-1$. For the aspect ratio $\Gamma=12$ considered here the dominant axial mode index in the decomposition (2.5) is $n=\pm 8$.

an unrolled cylindrical φ-z surface (that is, azimuthally extended to 4π for better visualization) by gray scale plots. The bottom contains snapshots of the node positions of u at midgap. These snapshots cover a time interval of about 100 radial diffusion times. The snapshot times are marked in Fig. 3, which exhibits the dynamics of the dominant characteristic mode amplitudes for TVF ($M=0$) and SPI ($M=\pm 1$), respectively.

Snapshot (A) in Fig. 2 shows that by this time the rotational symmetric TVF state has been established in the bulk. The Ekman vortices of higher flow intensity are marked by the brightest outflow line near each lid. By the time (B) the $m=\pm 1$ modes that break the rotational symmetry have grown sufficiently to see the wavy deformation of the still dominant $M=0$ TVF in snapshot (B). Here the amplitudes of $m=1$ and $m=-1$ modes are still of equal size, giving rise to an azimuthally rotating modulation of the TVF almost harmonic behavior. Then the amplitudes of the $m=1$ and $m=-1$ modes start to oscillate in counterphase with growing oscillation amplitude while the $m=0$ mode does not change much, cf. Fig. 3. But shortly before snapshots (C), the $m=1$ L-SPI mode takes off, it continues to increase while the $m=-1$ R-SPI mode and also the $m=0$ mode decrease.

This mode behavior reflects the fact that by starting in the bulk the TVF vortices become more and more deformed. The nodes of u in the bottom part of Fig. 2 show how the vortices approach each other [cf. arrows in (C)] and get pinched together at a defect that "cuts" them into two. They move apart [cf. arrows in (D)], get tilted in the φ-z plane of Fig. 2, and reconnect differently to locally form a spiral vortex pair. This defect formation and reconnection is repeated at two new locations further upward and downward toward the lids. The defect propagation is stopped by the strong Ekman vortex structures. They are only slightly indented by the rotating defect in the final state.

So, in the final state at time (H), the bulk is filled with an axially upward propagating L-SPI structure. Its phase is generated by a defect that is rotating in the lower part of the system. The spiral phase is annihilated at another rotating defect in the upper part of the system.

Here the $m=1$ mode wins the mode competition, leading finally to a L-SPI structure in the bulk, while the $m=-1$ mode gets suppressed, which is not due to an intrinsic selection mechanism. It merely reflects the fact that in this particular transient the initial white noise condition of the velocity field had a slightly higher content of L-SPI modes. In other runs with another noise realization, the R-SPI could equally well win the competition given that our random number generator for producing the white noise is unbiased.

B. Steady state structure and dynamics

By the time (H) in Fig. 2, transients have died out and the flow has reached its final state. It consists of an L-SPI structure in the bulk with the azimuthal wave number $M=1$ (i.e., one pair of spiral vortices), slightly modulated Ekman vortex structures that are localized next to the two lids, and two rotating but axially not propagating defects. This flow structure is rotating as a whole, like a rigid body with a global rotation rate ω into the same positive φ direction as the inner cylinder. However, the spiral rotation rate ω is somewhat smaller than the one of the inner cylinder [24]. Driven by this rotation the L-SPI phase in the bulk is propagating axially upward.

We should like to stress that the flow in Fig. 2(H) contains in the decomposition (2.5) besides the dominant $m=1$ SPI modes, not only $m=0$ modes that are related primarily to the Ekman vortex structures, but also a significant $m=-1$ contribution, cf. Fig. 3. The rotating defects and the rotating modulations of the Ekman vortices are the reason for the presence of $m=-1$ modes in addition to $m=1$ modes. In fact, locally, in the axially nonpropagating flow regions of the rotating defects and of the rotating Ekman vortex modulations, they combine to axially standing oscillations.

1. Structure of the rotating defects

The Ekman vortices near the lids do not propagate but remain spatially localized while the SPI vortices propagate. The connection between these topologically different vortex structures is provided by a pair of rotating defects: The one close to the lower Ekman vortex structure generates the L-SPI phase where two lines of nodes of the SPI u field appear in Fig. 2(H) in the form of a U tilted to the left. The defect close to the upper Ekman vortex structure annihilates the phase when the lines of the SPI nodes join again. With the two defects located at the beginning and end, respectively, of the spiral vortex pair, the former may be seen as pinning the latter.

The flow structure in the vicinity of the two rotating defects is shown in Fig. 4 for $R_1=115$. The gray scale plots show from top to bottom u, w, and the intensity $I=\sqrt{u^2+w^2}$ over the φ-z plane. The left (right) column documents the L-SPI generation (annihilation) near the lower (upper) Ekman vortex structure. The zeroes of u and w are shown by thick lines. Their U-turn marks the location of the defects. The phase-generating defect in the three fields of the left column that disrupts the bottom Ekman vortex structure has a slightly more complex structure than the phase annihilating defect in the right column. One sees that the Ekman vortices closest to the lids are modulated by the rotating defect but otherwise remain intact. Figures 2(H) and 4 also show that the upward propagating spiral vortices compress the Ekman vortex structure near the upper lid and dilate the one near the lower lid. Thus, the upwards traveling SPI phase "pushes" the Ekman vortices toward the top lid and "pulls" them away from the bottom lid.

Figure 5 shows in more detail the spatiotemporal dynamics of generation, propagation, and annihilation of SPI vortices over one period. To that end, snapshots of the azimuthal vortex flow field v-v_{CCF} are taken in the z-r plane at fixed φ at times $t_n\omega=2\pi n/16$ or, equivalently, at fixed t at azimuthal angles $\varphi_n=2\pi n/16$. In snapshots 1–8 the fourth vortex from the left, $z=0$, expands. Then, at $n=8$-9 a new one starts to grow close to the inner cylinder, thereby marking the defect. In snapshots 10–14, this new vortex continues to grow and to expand toward the outer cylinder. Simultaneously, at $n=9-11$ the old fourth vortex splits into two single vortices with the same direction of rotation—one to the left and one

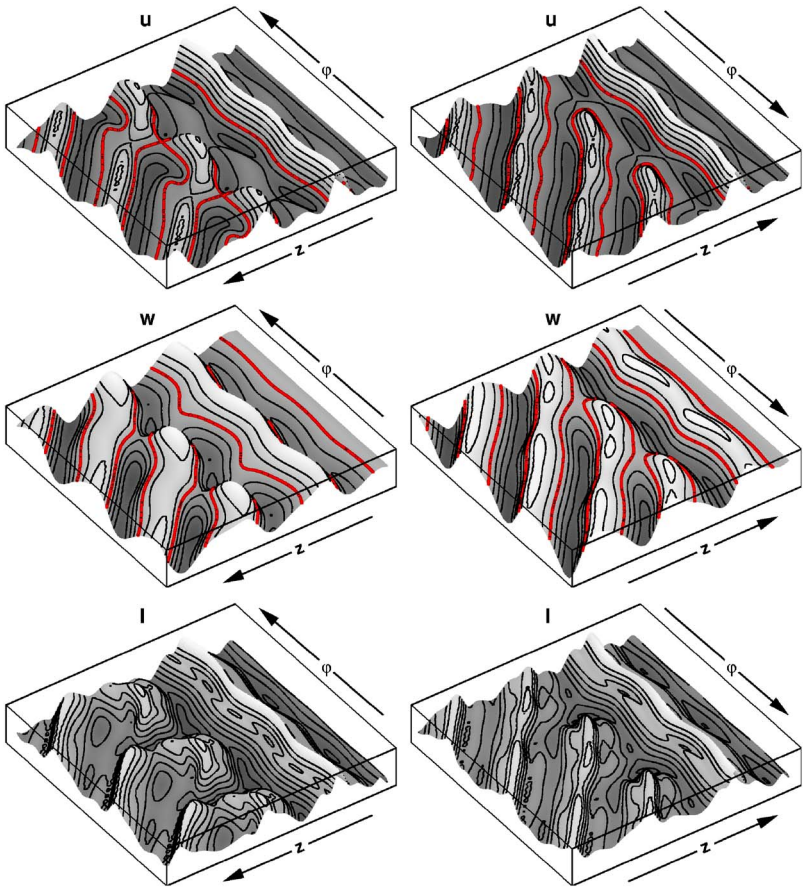

FIG. 4. (Color online) Flow structure in the vicinity of the rotating defects. The left (right) column documents the L-SPI generation (annihilation) near the lower (upper) Ekman vortex structure. Shown are the fields u, w, and $I=\sqrt{u^2+w^2}$ at midgap over the φ-z-plane. Note that there is only one defect at top and bottom: for better visibility the plots are periodically extended to an azimuthal interval of 4π. Thick isolines in the u, w plots show the node positions of these fields. Parameters are $R_1=115$, $R_2=-100$, and $\Gamma=12$.

to the right of the new one. The right neighbor is displaced upward and propagates away. Vortex annihilation proceeds by squeezing the fourth vortex from the top say, at $n=9-10$ and by merging its two neighbors in snapshots 10–12.

For $R_1=110$ [Fig. 2(H)], i.e., close to the SPI bifurcation threshold the axial extension of the spiral region is not as large as for $R_1=115$ (Fig 4). In fact, in the range $110\leqslant R_1\leqslant 117$, the bulk SPI region increases with increasing R_1 by displacing the Ekman vortex structures as the SPI amplitudes grow. Even stronger rotation speeds $R_1>117$ however, seem to prefer TVF; spirals are more and more displaced out of the boundary region.

2. SPI versus TVF modes

In Fig. 6 we show axial profiles of the dominant contributions in the decomposition (2.4) of the velocity fields from TVF and SPI modes. Full (dotted) lines show snapshots of the real parts of $m=0$ TVF ($m=1$ SPI) Fourier modes of u and w at midgap in systems of different length Γ.

One sees that for the fixed $R_1=115$ shown in Fig. 6, the extension of the $m=0$ Ekman vortex systems into the bulk and their structure remain unchanged when Γ is changed. However, at $\Gamma\simeq 10$, the tails of the exponentially decreasing Ekman vortex flow created by the two lids start to visibly overlap in the bulk.

On the other hand, the axial extension of the SPI vortex structure (dotted lines) in the bulk adjusts itself to the cylinder length. The amplitude of the $m=1$ SPI mode is constant in the bulk and it decays exponentially toward the lids, but it reaches well into the Ekman vortex dominated region. This behavior reflects the rotating modulation of the Ekman vortices that is caused by the rotating defect between SPI and Ekman vortices. To sum up: decreasing the cylinder length shrinks the bulk range where spirals exist.

3. SPI wave number and frequency selection

Figure 6 indicates that the SPI structure at midheight (that is defined in Fig. 6 to lie at $z=0$ for presentation reasons) is the same, irrespective of the length of the system, over a wide range of Γ. The observation of such a unique selection of the SPI structure is corroborated by the fact that the SPI wave number k measured in the vicinity of the midheight position is practically independent of Γ, cf. top plot of Fig. 7. The selected SPI wave number varies between $k=3.47$, $\lambda=2\pi/k=1.81$ ($\Gamma=16$), and $k=3.57$, $\lambda=1.76$ ($\Gamma=10$).

Here it is worth mentioning that the corresponding SPI wavelength of $\lambda\simeq 1.76$ has been observed in experiments [18] done in a system of length $\Gamma=12$. Furthermore, the numerically determined SPI flow structure agrees almost perfectly with the one obtained by the afore-mentioned laser-Doppler velocimetry measurements, cf. Fig. 8 of Ref. [24]. The selected frequency is $\omega\simeq 30.3$ so that the SPI phase propagates axially with phase velocity $\omega/k\simeq 8.6$.

Figure 7 shows the results of a numerical simulation in which the length Γ was ramped down from $\Gamma=16$ to $\Gamma=5$ in

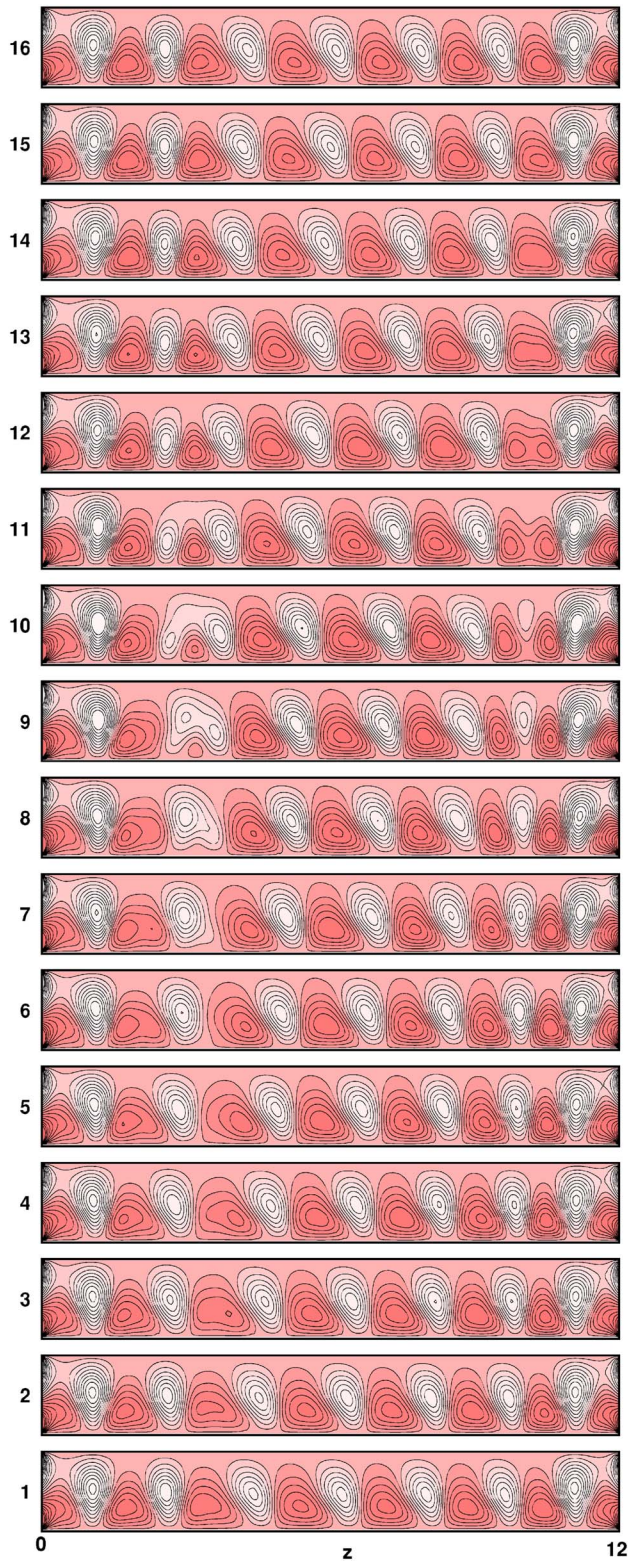

FIG. 5. (Color online) Steady state L-SPI generation, propagation, and annihilation covering one period. Shown are coded snapshots of the azimuthal vortex flow field v-v_{CCF}, together with its isolines in the z-r plane. They are taken at fixed φ at times $t_n\omega=2\pi n/16$ or, equivalently, at fixed t at azimuthal angles $\varphi_n=2\pi n/16$ for $n=1-16$ as indicated. The inner (outer) cylinder is located at the bottom (top) of each snapshot. Parameters are $R_1=110$, $R_2=-100$, and $\Gamma=12$ as in Figs. 2 and 3.

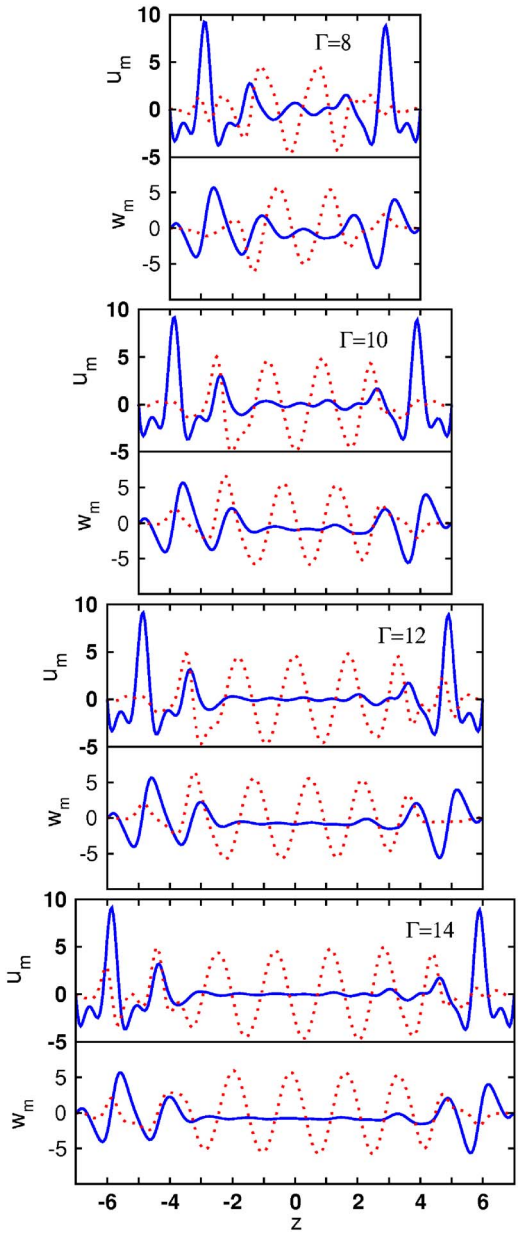

FIG. 6. (Color online) Axial profiles of the dominant contributions in the decomposition (2.4) of the velocity fields from TVF and SPI modes. Solid (dotted) lines show snapshots of the real parts of $m=0$ TVF ($m=1$ SPI) Fourier modes of u and w at midgap in systems of different length Γ. Parameters are $R_1=115$, $R_2=-100$.

steps of $\Delta\Gamma=0.05$ by moving the top lid downward. The time intervals between successive steps were about two radial diffusion times so that the SPI phase had always enough time to propagate from one end to the other.

In the bottom plot of Fig. 7 we show for each Γ the axial distribution of the nodes of u by dots. The nodes were monitored at discrete times during this time interval at a fixed φ. So, for example, the broadened lines near the top and bottom lids denote the narrow axial excursions of the locations of the Ekman vortices being modulated by the rotating defects. On the other hand, the homogeneously distributed dots in the center reflect the propagating SPI phase. The error bars in the top plot come from: (i) the finite sampling rate, which, in

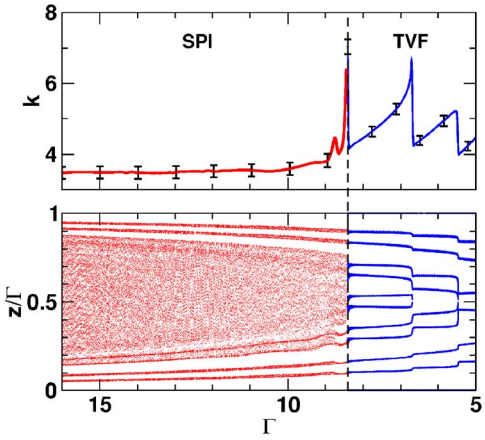

FIG. 7. (Color online) Spatiotemporal properties of the vortex flow as a function of system length. Γ was ramped down in steps of 0.05 by moving the top lid downward with about two radial diffusion times between successive steps. For each Γ the nodes of u were monitored during this time interval at discrete times at a fixed φ. Bottom plot shows the axial distribution of these nodes by dots, cf. text for further information and discussion. Top plot shows the wave number in the vicinity of mid-height location $z=\Gamma/2$ together with error bars explained in the text. The vertical dashed line marks the transition from SPI in the center part to TVF in this ramp "experiment." Parameters are $R_1=115$, $R_2=-100$.

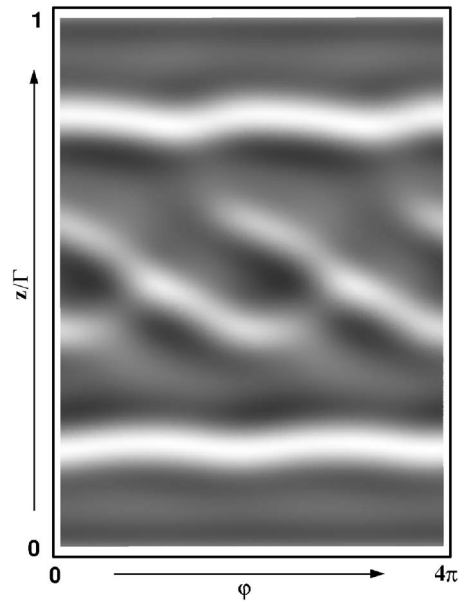

FIG. 8. Rotating defected vortex structure in a short system, $\Gamma=5.85$. Gray scale plot shows the radial velocity field u in an unrolled cylindrical φ-z surface at midgap. White (black) denotes radial out (in) flow. For better visibility the plot is periodically extended to an azimuthal interval of 4π. Parameters are $R_1=115$, $R_2=-100$.

general, is not commensurate with the time period of the propagating structure and (ii) from the fact that the nodes of u which are used to measure the wavelength lie (depending on that incommensurability) somewhere in a region around midheight.

We observed the same SPI frequency and wave number selection also in the upward ramp described in Sec. III C 2. Starting with TVF at small Γ, the SPI appeared there only at $\Gamma\simeq 10$. So whenever SPI flow was realized in a substantial part of the system with homogeneous amplitude, then its frequency and wave number was uniquely selected within our numerical accuracy.

C. Stability of SPI flow

1. Decreasing Γ

When in the described ramping "experiment" the length has fallen below $\Gamma\simeq 8.3$ the system has become too small to allow for a propagating SPI phase in the center. Instead, stationary $M=0$ Ekman and TVF is realized throughout the system with ten nodes in the bulk, cf., right part of Fig. 7. Reducing Γ further, the Taylor vortices become compressed, cf., the wave number plot. Then the number of nodes of u reduces to eight and finally to six as a vortex pair is annihilated in the center and then yet another one also is annihilated. The compression prior to the vortex pair annihilation and the relaxation to the old k value after the annihilation can be seen in the top plot of Fig. 7.

2. Increasing Γ

We also did a reverse ramp simulation in which the length was increased by moving the top lid upward from $\Gamma=5$ to $\Gamma=16$, starting from TVF with very small admixtures of $m\neq 0$ modes as they are still present shortly after a start from rest. The time intervals between upward steps of $\Delta\Gamma=0.05$ were two radial diffusion times. This time interval, however, is not long enough to allow for the full development of the spiral generating defects that are described in detail in Sec. III B. Here the SPI flow permanently reappeared in the center only at $\Gamma\simeq 10$ whereas it had disappeared in the downwards ramp at $\Gamma\simeq 8.3$. In addition, we found in the ramp simulations that the Γ values at which the transitions from SPI to TVF (and vice versa) occurred are also affected by the relative directions of the lid motion and the SPI propagation. The reasons for this hysteresis are on the one hand the upward ramp being too fast, but also an inherent bistability between TVF and SPI flow in this small system that is suggested by the following simulation.

3. Different initial conditions

Here we started with a perfect, axially periodic L-SPI structure of wavelength $\lambda=1.6$ at $R_1=115$, $R_2=-100$. Then we imposed instantaneously the rigid-lid boundary conditions at $z=0$ and $z=\Gamma=5.85$. Soon a defected vortex structure appeared (cf., Fig. 8) that rotates as a whole, like a rigid body. But the phase propagates axially upward only in a very small central region where the white stripes in Fig. 8 are tilted to the left. The time evolution of the six largest mode amplitudes $|u_{m,n}|$ (2.5) of the radial velocity field at midgap toward this final state are shown in Fig. 9. This vortex solution is dominated by the $m=0$ modes from the Ekman vortices. Then it contains $m=1$ modes with L-SPI character, but there is also a significant admixture of $m=-1$ modes with R-SPI character.

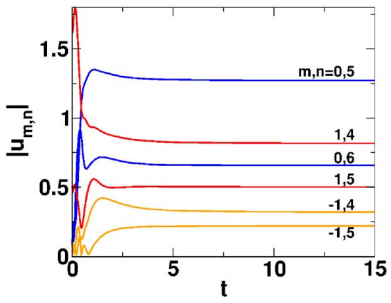

FIG. 9. (Color online) Time evolution toward the defected vortex state of Fig. 8. Shown are dominant mode amplitudes $|u_{m,n}|$ (2.5) of the radial velocity field at midgap. Here a perfectly periodic L-SPI structure was instantaneously subjected to rigid-lid boundaries at $z=0$ and $z=\Gamma=5.85$.

4. Remarks

Obviously the control parameter range in the R_2-R_1 plane of Fig. 1, in which SPI are stable in finite length systems, depends on Γ. Reducing Γ will shrink the range of SPI flow eventually to zero because of the ever present Ekman vortices in finite-length systems. In addition, the Ekman vortices also prevent the full stability domain of SPI under axially periodic conditions when Γ is increased. For example, at $R_2=-100$ we could not obtain stable SPI flow for $R_1 \gtrsim 123$, i.e., in a domain where SPI solutions coexist bistably with TVF solutions when axially periodic boundary conditions prevent Ekman vortices.

We checked that our numerically obtained stability boundaries largely agree with experimental ones [18]. But in the above-described downwards ramp simulation, we do not see SPI for $\Gamma < 8.3$ and, in particular, not at $\Gamma=5.85$ (where they are reported, e.g., for our $R_1=115$, $R_2=-100$ in Fig. 3 of Ref. [23]), but rather TVF, i.e, a pure $M=0$ stationary state. However, when starting from different initial conditions with different histories we do see SPI-like phase propagation with several modes being present. Thus, there seems to be multi- or at least bistability of pure $M=0$ vortex flow states coexisting with mixed-mode ones.

We mention that the way SPI flow in the center is destroyed or generated depends on the way the relevant parameters, say, R_1 and Γ are varied. In Fig. 7, Γ was decreased quasistatically, causing a reduction of the SPI extension that was almost quasi-static except for the last instance. What happened there can be better observed in a different simulation: starting at $R_1=115$ with stable L-SPI in a long system, the inner Reynolds number is stepped up instantaneously into the instability range of SPI flow, $R_1 \gtrsim 120$. Then a fast TVF front propagates upward. It originates from the Ekman vortex structure and it pushes the SPI phase-generating defects upward. The Ekman vortex structure at the upper lid, however, is unable to trigger a downward propagating TVF front against the upward traveling L-SPI phase. In fact, the phase annihilating defect below the upper Ekman vortex structure seems to be more robust. Finally, there could arise local wavy vortex flows at large enough R_1 or TVF. But we have also observed for smaller R_1 counter propagating spirals which originate from a defect in the center.

IV. CONCLUSION

We have numerically investigated how SPI flow is realized in finite length Taylor-Couette systems in which stationary top and bottom lids close the annulus, i.e., in the presence of spatially localized Ekman vortices. Results are presented for several system lengths $5 \leqslant \Gamma \leqslant 16$. In the parameter range investigated here, SPI solutions are stable under axially periodic boundary conditions. But TVF solutions would be unstable there under these idealized conditions without Ekman vortices. The presence of the latter in real systems tends to stabilize TVF and to destabilize SPI flow.

For example, in a start-from-rest simulation with small initial noise one can observe the following scenario First, on a short time scale of one to two radial diffusion times, the unstable CCF is growing radially in the bulk and simultaneously Ekman vortices are growing near the lids. Then fast TVF fronts propagate axially into the bulk from the Ekman vortex structures. Thereby unstable CCF is replaced by TVF within a few diffusion times. For those parameters for which this TVF is unstable in finite systems, one can then observe a slow transformation of TVF to SPI flow. Therein a pair of bulk TVF vortices becomes more and more deformed and gets pinched together at a defect that "cuts" them into two. They move apart, get reoriented, and reconnect differently to locally form a spiral vortex pair. This defect formation and reconnection is repeated at two new locations further upward and downward towards the lids. Finally, the axial defect propagation is stopped by the strong Ekman vortex structures.

In the final state the bulk is filled with, say, an axially upward propagating L-SPI structure. Its phase is generated by a defect that is rotating in the lower part of the system. The spiral phase is annihilated at another rotating defect in the upper part of the system. The Ekman vortex structures are only slightly indented and modulated by the respective rotating defect. The whole flow structure is rotating as a whole, like a rigid body with a global rotation rate into the same positive φ direction as the inner cylinder.

The SPI structure in the bulk is uniquely selected. Its wave number is for large system lengths practically independent of Γ, showing a slight variation only near the transition to TVF at small Γ. When changing quasistatically the system length at fixed R_1, R_2, the axial extension over which SPI flow is realized in the bulk changes accordingly. The Ekman vortex structures, on the other hand, remain basically unaffected. Below a critical Γ the two Ekman vortex structures have come too close to allow for SPI flow any more.

It would be interesting to quantitatively test the frequency and wave number selection in the SPI bulk, the structural dynamics of the rotating defects, and the interpenetrating SPI and Ekman vortex modes by spatiotemporal Fourier analyses of experimental data.

ACKNOWLEDGMENT

This work was supported by the Deutsche Forschungsgemeinschaft.

[1] For an account of the early history see, e.g., ref. [2]. Later reviews are contained in refs. [3–6].
[2] R. J. Donnelly, Phys. Today **44**(11), 32 (1991).
[3] R. C. DiPrima and H. L. Swinney, in *Hydrodynamic Instabilities and the Transition to Turbulence*, edited by H. L. Swinney and J. P. Gollub, Topics in Applied Physics Vol. 45 (Springer-Verlag, Berlin, 1985), p. 139.
[4] M. C. Cross and P. C. Hohenberg, Rev. Mod. Phys. **65**, 851 (1993).
[5] R. Tagg, Nonlinear Sci. Today **4**, 1 (1994).
[6] P. Chossat and G. Iooss, *The Couette-Taylor Problem* (Springer, Berlin, 1994).
[7] Y. Demay and G. Iooss, J. Mec. Theor. Appl. Spec. Suppl., 193 (1984).
[8] H. R. Brand, Phys. Rev. A **31**, 3454 (1985).
[9] S. Zaleski, P. Tabeling, and P. Lallemand, Phys. Rev. A **32**, 655 (1985).
[10] C. D. Andereck, S. S. Liu, and H. L. Swinney, J. Fluid Mech. **164**, 155 (1986).
[11] M. Golubitsky and I. Stewart, SIAM J. Math. Anal. **17**, 249 (1986); M. Golubitsky and W. F. Langford, Physica D **32**, 362 (1988).
[12] W. F. Langford, R. Tagg, E. Kostelich, H. L. Swinney, and M. Golubitsky, Phys. Fluids **31**, 776 (1988).
[13] R. Tagg, W. S. Edwards, H. L. Swinney, and P. S. Marcus, Phys. Rev. A **39**, 3734 (1989).
[14] W. S. Edwards, in *Instability and Transition*, edited by M. Y. Hussaini (Springer, Berlin, 1990), Vol. II, p. 408.
[15] W. S. Edwards, R. P. Tagg, B. C. Dornblaser, and H. L. Swinney, Eur. J. Mech. B/Fluids **10**, 205 (1991).
[16] E. Knobloch and R. Pierce, in *Ordered and Turbulent Patterns in Taylor-Couette Flow*, edited by C. D. Andereck and F. Hayot (Plenum Press, New York, 1992), p. 83.
[17] J. Antonijoan, F. Marquès, and J. Sánchez, Phys. Fluids **10**, 829 (1998).
[18] A. Schulz and G. Pfister, in *Physics of Rotating Fluids*, edited by C. Egbers and G. Pfister, Lecture Notes in Physics Vol. 549 (Springer, Berlin, 2000), p. 37; (unpublished).
[19] Ch. Hoffmann and M. Lücke, in *Physics of Rotating Fluids*, edited by C. Egbers and G. Pfister, Lecture Notes in Physics Vol. 549 (Springer, Berlin, 2000), p. 55.
[20] A. Meseguer and F. Marques, J. Fluid Mech. **455**, 129 (2002).
[21] O. Czarny, E. Serre, P. Bontoux, and R. Lueptow, Theor. Comput. Fluid Dyn. **16**, 5 (2002).
[22] A. Pinter, M. Lücke and Ch. Hoffmann, Phys. Rev. E **67**, 026318 (2003).
[23] J. Langenberg, G. Pfister, and J. Abshagen, Phys. Fluids **16**, 2757 (2004).
[24] Ch. Hoffmann, M. Lücke and A. Pinter, Phys. Rev. E **69**, 056309 (2004).
[25] E. R. Krueger, A. Gross, and R. C. DiPrima, J. Fluid Mech. **24**, 521 (1966).
[26] H. A. Snyder, Phys. Fluids **11**, 728 (1968); H. A. Snyder, *ibid.* **11**, 1599 (1968).
[27] G. Pfister and I. Rehberg, Phys. Lett. **83**, 19 (1981).
[28] R. Graham and J. A. Domaradzki, Phys. Rev. A **26**, 1572 (1982).
[29] G. Ahlers, D. S. Cannell, M. A. Dominguez-Lerma, and R. Heinrichs, Physica D **23**, 202 (1986).
[30] O. Czarny, E. Serre, P. Bontoux, and R. Lueptow, Phys. Fluids **15**, 467 (2003).
[31] P. J. Blennerhassett and P. Hall, Proc. R. Soc. London **365**, 191 (1979).
[32] J. Langenberg, G. Pfister, and J. Abshagen, Phys. Rev. E **68**, 056308 (2003).
[33] M. Lücke, M. Mihelcic, and K. Wingerath, Phys. Rev. A **31**, 396 (1985).